Cation diffusion and hybridization effects at the Mn-GaSe(0001) reacted interface: *Ab initio* calculations and soft x-ray electron spectroscopy studies

S. Dash,[1,2,3] N. Joshi,[4] G. Drera,[1] P. Ghosh,[4] E. Magnano,[5] F. Bondino,[5] P. Galinetto,[6] M. C. Mozzati,[6] G. Salvinelli,[1] V. Aguekian,[7] and L. Sangaletti[1]

[1]*Interdisciplinary Laboratories for Advanced Materials Physics (I-Lamp) and Dipartimento di Matematica e Fisica, Università Cattolica, via dei Musei 41, 25121 Brescia, Italy*

[2]*School of Material Science and Engineering, Nanyang Technological University, Singapore*

[3]*Singapore Synchrotron Light source, National University of Singapore, Singapore*

[4]*Indian Institute of Science Education and Research Pune, Maharashtra 411008, India*

[5]*IOM-CNR, Laboratorio TASC, S.S. 14, Km 163,5 I-34149 Basovizza, Italy*

[6]*CNISM and Dipartimento di Fisica, Università di Pavia, Via Bassi 6, Italy*

[7]*Solid State Physics Department, V. Fock, Institute of Physics, Saint-Petersburg State University, Petrodvoretz, 198904 S.-Petersburg, Russia*

(Received 20 March 2013; revised manuscript received 1 February 2016; published 9 March 2016)

The electronic properties of the Mn:GaSe interface, produced by evaporating Mn at room temperature on a ϵ-GaSe(0001) single-crystal surface, have been studied by soft x-ray spectroscopies, and the experimental results are discussed at the light of *ab initio* DFT+U calculations of a model $Ga_{1-x}Mn_xSe$ ($x = 0.055$) surface alloy. Consistently with these calculations that also predict a high magnetic moment for the Mn ions (4.73–4.83 μ_B), XAS measurements at the Mn L edge indicate that Mn diffuses into the lattice as a Mn^{2+} cation with negligible crystal-field effects. *Ab initio* calculations also show that the most energetically favorable lattice sites for Mn diffusion are those where Mn substitutes Ga cations in the Ga layers of the topmost Se-Ga-Ga-Se sandwich. Mn s and p states are found to strongly hybridize with Se and Ga p states, while weaker hybridization is predicted for Mn d states with Se s and p orbitals. Furthermore, unlike other Mn-doped semiconductors, there is strong interaction between the Ga-s and Mn-d_{z^2} states. The effects of hybridization of Mn 3d electrons with neighboring atoms are still clearly detectable from the characteristic charge-transfer satellites observed in the photoemission spectra. The Mn 3d spectral weight in the valence band is probed by resonant photoemission spectroscopy at the Mn L edge, which also allowed an estimation of the charge transfer ($\Delta = 2.95$ eV) and Mott-Hubbard ($U = 6.4$ eV) energies on the basis of impurity-cluster configuration-interaction model of the photoemission process. The Mott-Hubbard correlation energy U is consistent with the U_{eff} on-site Coulomb repulsion parameter (5.84 eV) determined for the *ab initio* calculations.

DOI: 10.1103/PhysRevB.93.115304

I. INTRODUCTION

The III-VI semiconductors GaSe, InSe, GaTe, and GaS are known for their remarkable nonlinear optical properties, which make them quite interesting materials for photo-electronic applications [1–5], even in the form of nanowires [6]. In the particular case of GaSe and GaS, the interest on these systems has been recently renewed by the search for graphene analogues in layered materials [7,8]. Studies on pure and doped monolayers and nanosheets have been recently reported [9,11–15] and the possibility to obtain ultrathin layer transistors based on atomic-thin sheets has been demonstrated [16]. Nanostructured GaSe in the form of nanotubes was also predicted [17], along with the possibility to strain-engineer ϵ-GaSe layers to obtain a topological insulator [18]. Recently, GaSe and GaS were also considered as templates for the growth of silicene layers [19].

When doped with transition metal ions (e.g., Mn [20], or Fe [21]-doped GaSe), the III-VI semiconductors display interesting magnetic properties, addressing further studies aimed to identify new classes of diluted magnetic semiconductors of the form $A^{\text{III}}_{1-x}M_xB^{\text{VI}}$, where $A^{\text{III}}B^{\text{VI}}$ is a III-VI semiconductor and M is a transition metal ion. For instance, Mn has been incorporated into GaSe(0001) in crystals grown from the melt, and intriguing magnetic properties have been found [20] that may be rationalized by considering a possible interplay between doping and magnetism [22]. A short-range antiferromagnetic ordering has also been invoked to explain the rather complex magnetic behavior, but a clear identification of the short-range coupling mechanisms related to these experimental evidences is still missing. Moreover, a clear understanding of the interplay between magnetism and electronic properties has not yet been reported so far, mainly due to the difficulty of growing high quality Mn-doped single crystals and control both the doping level and possible phase segregations or the creation of defects and vacancies upon doping. Also the local structure around Mn atoms at the Mn:GaSe interface has not yet been probed, being the mechanism of Mn diffusion in the lattice poorly investigated. This can be important in order to relate the observed magnetic behavior to either direct or superexchange interactions through Mn–Mn or Mn–Se–Mn bonds, respectively. Furthermore, recent studies [23,24] have drawn the attention on the Mn:Ga_2Se_3 interface, that is strictly related to the one we are currently studying and displays weak antiferromagnetic correlations in the bulk crystal [25].

Substitutional magnetic ions (e.g., Mn) in the III-VI diluted magnetic semiconductors (DMS) are found in a trigonal (distorted tetrahedral) environment, ultimately related to the tetrahedral environment typical of these ions in II-VI compounds. However, in sharp contrast to the II-VI DMS, the III-VI semiconducting host presents a two dimensional (2D) nature, at the origin of the renewed interest in ultrathin layers

of, e.g., GaSe and GaS [16]. The two-dimensional nature of these crystals is determined by the weak van der Waals bonding between the stacked four-atom thick layers (e.g., Se-Ga-Ga-Se in GaSe).

GaSe had also been a quite popular layered semiconductor material in the 70's because it revealed a switching effect and was considered as an alternative to Ovshinsky switching diode [26]. Early electronic structure calculations of GaSe are reported in Ref. [27]. Because of its markedly nearly 2D structure, GaSe has also been considered in the past for angle-resolved photoemission (ARPES) experiments, and a recent study has renewed the interest on this aspect by providing high quality ARPES data supported by band structure calculations of the bulk crystal [28]. *Ab initio* calculations are now carried out mostly on few-layer GaSe sheets [29,30], and theoretical predictions of electronic and magnetic properties of hole-doped GaSe monolayers [31] have been recently reported. Electronic structure calculations have also been focused on strain effects in GaSe bulk [32] and few-layer systems [33], discussing the possibility to tune the band gaps of GaSe monolayers by mechanical deformation and to engineer novel tunable nanodevices.

Aimed to provide an experimental and theoretical reference for possible studies of ultrathin GaSe layers doped with magnetic ions, the present study is focused on the electronic properties of the Mn-GaSe interface obtained by evaporating Mn ions on the (0001) surface of a ultrahigh vacuum cleaved ϵ-GaSe single crystal. Doping of GaSe with Mn could then be further promoted by postgrowth annealing treatments in ultrahigh vacuum conditions.

In the recent years, this technique has been widely used in the field of DMS, as it allows to control doping level by finely tuning the evaporation rate and also to trigger diffusion mechanisms, as well as surface reconstructions by in-vacuum, postgrowth, annealing treatments. In the case of Mn, the result is a large variety of surface structures and ultrathin interfaces spanning a wide range of systems such as Mn on Si [34–36], Mn on Ge [37–42], Mn on CdTe [43,44], Mn on SiC [45], Mn on GaAs [46], Mn on $ZnGeP_2$ [47], and Mn on GaN [48]. The preparation of Mn-doped DMS through evaporation and annealing may introduce mechanisms that are not usually found in the growth of single crystals. Diffusion from the surface to substitutional or interstitial sites of the innermost layers, transition metal segregations at the surface, and in the specific case of GaSe, intercalation of Mn-rich layers between the weakly bond Se layers can therefore be expected. In the case of GaSe, the latter process has been reported for Fe evaporation [49,50], but not yet for Mn.

Room-temperature cation diffusion through the surface can also be regarded as an effective method to dope single or few layers in GaSe and similar 2D compounds, thus allowing to focus on the electronic properties of ultrathin layers. In fact, the possibility to control the evaporation rate at sub-ML scale allows one to accurately track effects at the surface that may have, with respect to bulk samples, a considerable weight in the physical properties of the system, as it can be composed of a single stack of few atomic layers (e.g., four layers in the case of GaSe). Being aware that, because of its layered structure, Mn doping of GaSe may display a more complex scenario with respect to the diamond like elemental semiconductors (Si, Ge) or the zinc-blende III-V and II-VI systems, we proceeded with our study in order to explore the electronic properties of the reacted Mn:GaSe interface.

In the first part, we tracked the evolution of the Mn-GaSe interface by evaporating at room temperature (RT) increasing quantities of Mn on the GaSe surface. In this way, we identified the interface growth regimes, and in particular the balance between cation diffusion through the surface and cation segregation at the surface. Once the interplay between these processes was assessed, we prepared a Mn:GaSe interface where the $Ga_{1-x}Mn_xSe$ surface alloying through cation diffusion is dominant over Mn segregation on the surface, and we studied the electronic properties through resonant photoemission and x-ray absorption spectroscopies.

The experimental results are compared with *ab initio* DFT+U calculations of a model $Ga_{1-x}Mn_xSe$ surface alloy. Substitutional Mn ions are predicted to be energetically favorable, in agreement with the analysis of the x-ray photoemission core level intensity versus Mn coverage at the early stages of growth. Hybridization effects between Mn orbitals and Ga and Se orbitals are discussed, and a different behavior between Mn 3d and Mn s and p states is evidenced. The Mn 2p-3d x-ray absorption spectrum shows that Mn diffuses in GaSe as a Mn^{2+} cation displaying low crystal-field distortions, which is consistent with *ab initio* calculation results that predict the half-filling of Mn 3d orbitals and the high magnetic moment (4.73–4.83 μ_B) characteristic of cations in low crystal fields.

II. EXPERIMENTAL AND COMPUTATIONAL DETAILS

The GaSe single crystals have been grown by the Bridgman method [51]. The crystals were cleaved in ultrahigh vacuum conditions prior Mn evaporation. Mn layers were deposited at RT by *in situ* electron beam evaporation from an outgassed Mo crucible loaded with metallic Mn flakes. An Omicron EFM-3 triple evaporator was used in all experiments. The deposition rate was properly calibrated before evaporation on the GaSe cleaved surface. Three interfaces have been produced during the experiments.

(i) The first interface was obtained by evaporating an increasing amount of Mn (from 0.8 ML up to 3.6 ML, with steps of 0.4 ML). Here 1 ML of Mn is defined as the number of atoms in the top layer of a GaSe crystal, i.e., 8×10^{14} atoms/cm^2 (according to M. Zerrouki *et al.* [55]). No post-growth annealing was carried out. The data collected from this interface are reported in the Sec. III A.

(ii) The second interface, described in the Sec. III B, was obtained by evaporating 4.6 ML of Mn, and by annealing the interface at 400 °C in ultrahigh vacuum for 10 minutes to favor the Mn diffusion process in the GaSe lattice.

(iii) The third interface (considered in the remaining sections) was produced at the BACH beamline, by depositing a sub-ML of Mn at room temperature. As in the previous case, a 10 minutes annealing in ultrahigh vacuum at 400 °C was carried out after the Mn evaporation.

X-ray absorption and resonant photoemission spectroscopy measurements were performed at the BACH beam line of the CNR at the Elettra Synchrotron Light Source. The x-ray photoemission (XPS) data have been collected at the Surface Science and Spectroscopy Lab of the Universitá Cattolica

(Brescia, Italy) with a nonmonochromatized dual-anode PsP x-ray source and a SCIENTA R3000 analyzer, operating in the transmission mode, which maximizes the transmittance and works with a 30° acceptance angle.

The surface sensitivity (XPS probe depth) at the various kinetic energies (KE) was evaluated by Monte Carlo calculations of the depth distribution function, based on the algorithm described in Ref. [52], in order to include both inelastic and elastic electron scattering, in the so-called transport approximation [53]. We define the calculated probe depth for photoemission as the maximum depth from which 95% of all photoemitted electrons can reach the surface. In case of exponential attenuation of the signal, this would correspond to three times the electron escape depth. When both the inelastic mean free path (IMFP) and the transport (elastic) mean free path (TMFP) are included in the calculations, a rough estimation of the electron escape depth can be provided by the effective attenuation depth ($1/\lambda_{\text{eff}} = 1/\lambda_{\text{IMFP}} + 1/\lambda_{\text{TMFP}}$). Details of the specific codes used to evaluate the electron escape depths can be found in Ref. [54].

The e-beam evaporator was calibrated by depositing Mn layers on a clean Si substrate, before replacing Si with GaSe and proceeding with ultra high vacuum GaSe cleaving and Mn evaporation, at the conditions used for Mn evaporation on Si. The thickness of the Mn layer was estimated by referring to the relative intensities of the Mn $3p$ and Si $2p$ core lines. The attenuation of the Si $2p$ signal was modeled with the BRIXIAS code [54], assuming a uniform metallic Mn layer growing on the Si wafer with a sharp interface. Both inelastic (IMFP) and elastic (TMFP) electronic scattering processes were considered within the Monte Carlo algorithm described by Werner in Ref. [52] in the transport approximation. The values for λ_{IMFP}, λ_{TMFP} and the effective attenuation depth (λ_{eff}) are listed in Table I. Once the thickness of the metallic Mn layer was estimated, this value was converted in Mn atoms/cm^2 and, according to the study of Zerroucky *et al.* [55], the surface density was finally converted into Mn ML deposited on the 0001 GaSe surface.

The Mn stoichiometry in GaSe was estimated for low Mn coverages (i.e., below about 1.5 ML), where the Mn diffusion in the GaSe lattice was shown to be much more likely than clustering of excess Mn at the surface. The aim of this estimation was to provide an input for the calculations, as the amount of Mn in the lattice affects the dimension of the supercell selected for the calculations. Actually, the Mn stoichiometry considered in the supercell calculations was $x = 0.055$, comparable to the value estimated through the analysis of XPS data ($x = 0.056 \pm 0.005$ in $Ga_{1-x}Mn_xSe$).

TABLE I. Electron scattering lengths in silicon and manganese. KE is the kinetic energy of photoelectrons emitted upon absorption of 1486.7 eV photons from the Al K_α x-ray line.

XPS core line	KE (eV)	Material	Density (g/cm^3)	λ_{IMFP} (Å)	λ_{TMFP} (Å)	λ_{eff} (Å)
Mn $3p$	1432	Metallic Mn	7.43	21.93	73.01	16.87
Si $2p$	1383	Silicon	2.33	30.85	250.39	27.47
		Metallic Mn	7.43	21.61	71.07	16.57

TABLE II. Electron scattering lengths in GaSe. KE is the kinetic energy of photoelectrons emitted upon absorption of 1486.7 eV photons from the Al K_α x-ray line.

XPS core line	KE (eV)	λ_{IMFP} (Å)	λ_{TMFP} (Å)	λ_{eff} (Å)
Se $3d$	1425	29.62	108.14	23.25
Mn $3p$	1432	29.73	108.83	23.35
Ga $3d$	1459	30.17	111.51	23.75

For this estimation, we considered a uniform distribution of Mn in the GaSe lattice and we considered the Mn $3p$, Ga $3d$, and Se $3d$ XPS peaks. The relative intensities were compared with theoretical predictions obtained by assuming a density of 5.03 g/cm^3 for GaSe. The IMFP, TMFP, and λ_{eff} values are listed in Table II. No diffractive effects were included in the calculations. Complete layer-resolved modeling of the actual concentration profile would require angle-resolved XPS experiments, where a consistent set of XPS spectra is collected at different take-off angles and different possible concentration profiles are explored, assisted by an input from an estimation of cation lattice energies and diffusion kinetics (see, e.g., Refs. [56,57] for recent layer-by-layer modeling of oxide heterointerfaces).

We have performed spin polarized density functional theory (DFT) based calculations using the Quantum Espresso software [58], which is an implementation of the DFT in a plane wave pseudopotential framework. The electron-ion interactions were described using ultrasoft pseudopotentials [59]. We have used a kinetic energy cutoff of 35 Ry and 400 Ry for the wave function and charge density respectively. The electron-electron exchange and correlation functional was described with the Perdew-Burke-Ernzerhof (PBE) parametrization of the generalized gradient approximation (GGA) [60]. To speed up convergence, we have used a Marzari-Vanderbilt smearing of 0.001 Ry [61].

ϵ-GaSe has a 2H stacking sequence, the unit cell extends over two sandwiches with hexagonal symmetry [Fig. 1(a)]. These sandwiches interact though weak van der Waals dispersion. This interaction is not included in the conventional PBE exchange-correlation functional. Hence we have used an empirical van der Waals correction [62,63] to the total energy. For the bulk structure Brillouin zone (BZ) integrations were done using a $8\times8\times4$ shifted Monkhorst-Pack [64] k-point grid. Our calculations yield the bulk lattice parameters a and c of ϵ-GaSe to be 3.74 and 15.88 Å, respectively. These are in excellent agreement with those reported in Ref. [65].

The (0001) surfaces are modeled using a slab where we have considered two sandwiches stacked along the (0001) direction and separated by vacuum along the (0001) direction [Fig. 1(b)]. Since the sandwiches interact through weak van der Waals interaction, when the (0001) surface is created through cleaving the crystal (as done in this work), the cleavage will take place in between two sandwiches, exposing the Se atoms to the surface. Therefore, in our model, the slab has a Se-termination on both sides. This has an added computational advantage. Since we are using periodic boundary conditions in our calculations, there is spurious interaction between the slab and its periodic images, through the surface dipole. Having Se

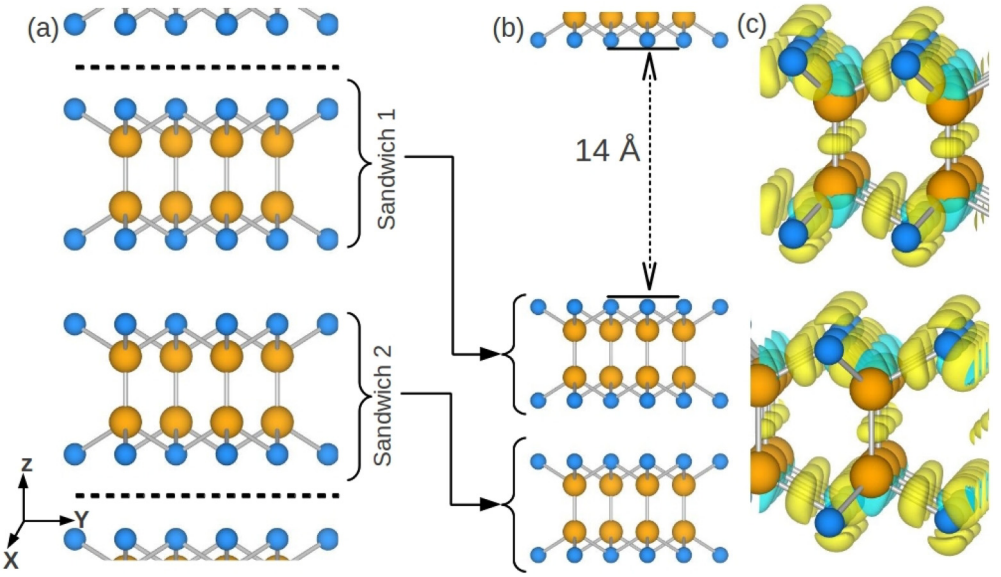

FIG. 1. (a) Structure and stacking sequence of bulk ϵ-GaSe. The dashed horizontal lines denote the periodically repeated unit along the z axis. (b) The slab model used to describe the (0001) surface of ϵ-GaSe. (c) The isosurfaces showing the difference between the computed charge density and that obtained from superposition of atomic charge density for bulk ϵ-GaSe. The blue and yellow spheres denote Se and Ga atoms, respectively. The yellow surfaces show accumulation of charge while the green ones show depletion of charge.

atoms on both the surfaces cancels this dipole and reduces the spurious interaction significantly. For our calculations we have used a vacuum of about 14 Å in the direction perpendicular to the surface. For the Mn-doped slabs, the symmetry of the surfaces on either side of the slab is broken. For these we incorporate a dipole correction to ensure that the electrostatic potential in the vacuum region is flat (for details see Ref. [86]). To study the effect of Mn doping in these systems, we have used a 3×3 surface unit cell and put one Mn atom resulting in a doping concentration of about 5.5%, which is similar to the experimental doping concentrations at low doping. The BZ integrations for the surface calculations were done using $2 \times 2 \times 1$ shifted k-point grid.

To correctly account for the strong Coulomb and exchange interactions between the Mn d electrons, we have used the DFT+U method. In this work, we have used the implementation of Cococcioni and Gironcoli as described in Ref. [66], which is an improved and rotationally invariant simplified form of the the DFT+U approach proposed by Anisimov and co-workers [67–69]. The effective on-site Coulomb repulsion parameter U_{eff} is determined using the linear response theory proposed by these authors [66]. This allows to calculate in an internally self-consistent way the U_{eff} without making prior assumptions about the screening and/or basis set used in the calculation. The U_{eff} can be calculated directly by the response function as follows:

$$\chi_{IJ} = \frac{\partial^2 E}{\partial \alpha_I \alpha_J} = \frac{\partial n_I}{\partial \alpha_J}, \tag{1}$$

where χ_{IJ} is obtained from the response of d state occupations to a small localized perturbation potential α. U_{eff} is then given by

$$U_{\text{eff}} = \left(\chi_0^{-1} - \chi^{-1}\right), \tag{2}$$

where χ_0^{-1} and χ^{-1} are the Kohn-Sham and the interacting inverse density response function of the system with respect to localized perturbations. By changing the rigid potential shifts α, we obtain the bare and the self-consistent occupation regression response functions, which are plotted in Fig. 2. The χ^{-1} and χ_0^{-1} are given by the slopes of the plots. From there we determine the U_{eff} to be 5.84 eV.

III. RESULTS AND DISCUSSION

A. Cation diffusion versus surface segregation

In Fig. 3(a), a sequence of Mn $2p$ XPS spectra collected after each Mn evaporation at RT on the freshly cleaved ϵ-GaSe

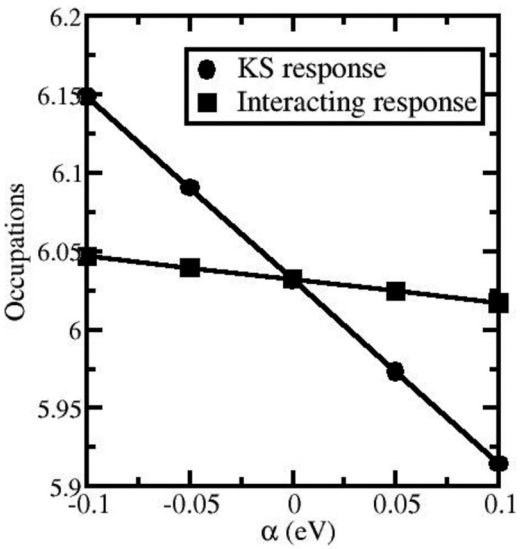

FIG. 2. Linear response of Mn-d occupation to the change of potential shift α.

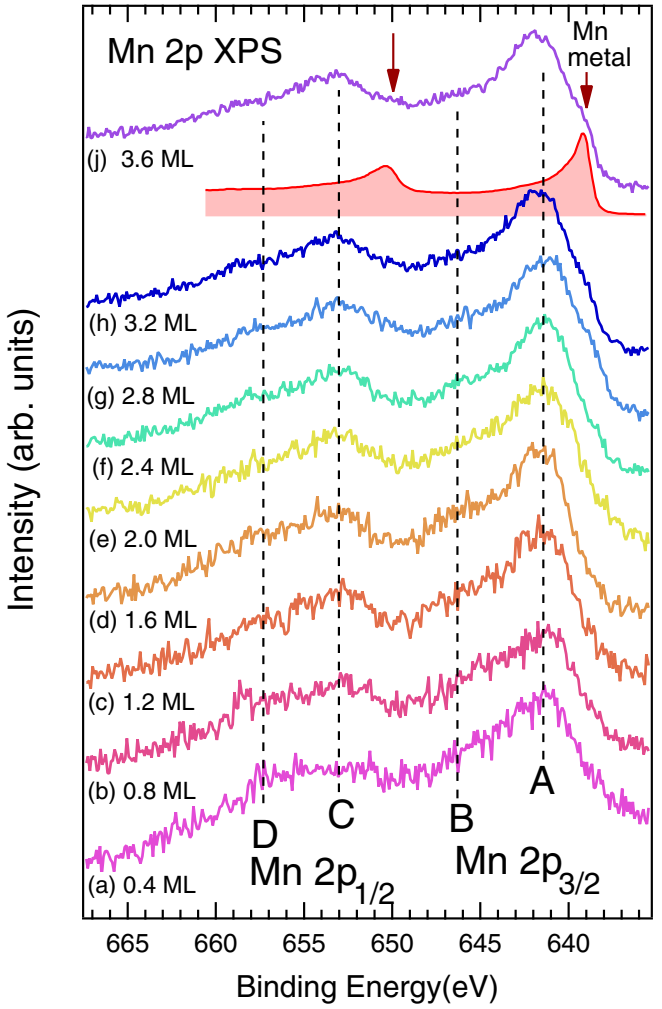

FIG. 3. Sequence of Mn $2p$ spectra collected with Al K_α photon source for Mn deposited on the ϵ-GaSe(0001) surface in steps, which added up to a thickness from 0.4 to 3.6 ML (incremental thickness: 0.4 ML after each step). The spectra have been normalized to the peak height of the Mn $2p_{3/2}$ component.

surface is shown, where the Mn $2p_{3/2}$ and Mn $2p_{1/2}$ spin-split features of the Mn $2p$ core line are detectable. Each spin-orbit split component is composed of two broad peaks, denoted as A and B for the $2p_{3/2}$ component, and C and D for the $2p_{1/2}$ component. These spectra are typical of Mn in DMS, as will be discussed in the next section. Furthermore, the overall Mn $2p$ line shape changes as the amount of deposited Mn increases. In particular, starting from spectrum (f) (2.4 ML) a peak ascribed to metallic Mn is clearly detectable on the low BE side of the Mn $2p$ main line, with a BE of 638 eV. The Mn $2p$ XPS spectrum of a Mn thick film is also shown below spectrum (j) (shaded area), to help identifying the contribution of metallic Mn in the data.

A set of shallow core levels (Se $3d$, Mn $3p$, and Ga $3d$) with much higher kinetic energies (about 1450 eV) has been collected. With this KE, the probe depth is about 7.0 nm for the three shallow core level emissions. On this basis, the Ga $3d$/Mn $3p$ and Se $3d$/Mn $3p$ ratio versus Mn film thickness are shown in Fig. 4. The experimental data are compared with the results expected for a uniform Mn coverage without any diffusion

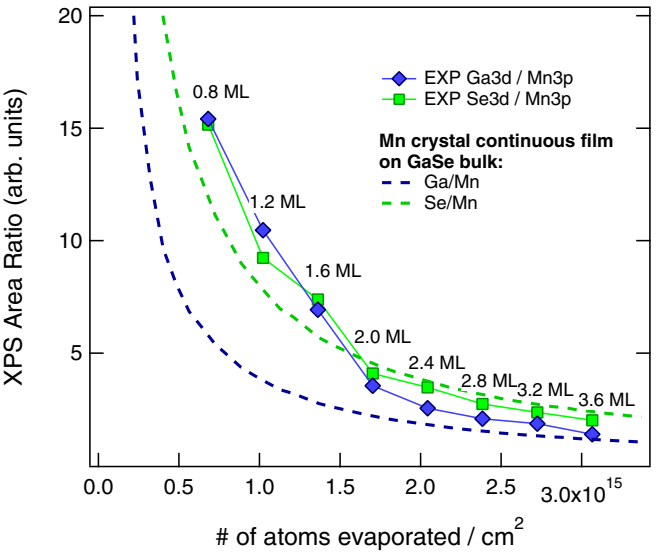

FIG. 4. Se $3d$/Mn $3p$ (filled squares) and Ga $3d$/Mn $3p$ (filled diamonds) peak area intensity ratios vs Mn nominal coverage (ML). Calculated ratios (dashed lines) assuming a Mn continuous film on GaSe.

and alloying process (dashed lines). As can be observed, only for larger coverages the measured data are fairly fit by the computational predictions, while for a Mn evaporation below about 2 ML, the measured signal attenuation is not as large as the predicted one. This is consistent with the hypothesis of diffusion mechanisms leading to a reacted surface layer before a uniform Mn coverage regime is established.

The Mn stoichiometry x in the $Ga_{1-x}Mn_xSe$ alloy was also estimated by measuring the intensity of the Mn $2p$ core level peak with respect to the Ga $3d$ and Se $3d$ core lines. After proper normalization to photoemission cross sections and analyzer transmission, assuming a uniform distribution of Mn ions through the topmost surface layers, the amount of Mn diffused into the crystal after 1.2 ML Mn evaporation (Fig. 3, spectrum c) resulted to be $x = 0.056 \pm 0.005$ in $Ga_{1-x}Mn_xSe$.

In order to determine the preferred Mn site, we considered five possibilities in our model: (a) Mn adsorbed on the surface, (b) Mn replacing the surface Ga atom, (c) Mn replacing a Ga atom in the second layer of the sandwich, (d) Mn intercalated between two sandwiches, and (e) Mn in an interstitial site. For (a), we considered two configurations, Mn in a bridge site between two Se atoms and Mn atop a Se atom. To compare the energetics of the five above mentioned possibilities, we considered the following reactions. For (a), (d), and (e) where no Ga atom is replaced with Mn, the following reaction is considered:

$$GaSe + Mn(g) \rightarrow GaSe + Mn, \quad (3)$$

where (g) denotes Mn atom in the gas phase. For (b) and (c), where Mn is replacing a Ga atom, we consider the following reaction:

$$GaSe + xMn(g) \rightarrow Ga_{1-x}Mn_xSe + xGa(\text{surface/interstitial}), \quad (4)$$

TABLE III. Energetics of the reactions considered to place Mn on the different possible lattice sites. FM and AFM denote ferromagnetic and antiferromagnetic coupling between two Mn impurities.

Model	Configuration	ΔE (eV)
Mn adsorbed on the surface	atop Se	3.75
	Se-Se bridge (FM)	0.42
	Se-Se bridge (AFM)	0.39
Mn replacing surface Ga atom	Ga on surface at the hollow site formed by three Se atoms (FM)	–0.95
	Ga on surface at the hollow site formed by three Se atoms (AFM)	–0.94
	Ga interstitial within the sandwich	–0.06
Mn replacing Ga atom atom in the second layer	Ga atom intercalated between two sandwiches (FM)	–0.64
	Ga atom intercalated between two sandwiches (AFM)	–0.63
	Ga interstitial within the sandwich	–0.03
Mn intercalated between Se layers	atop Se of the lower sandwich	0.15
	atop Ga of the lower sandwich (FM)	–0.01
	atop Ga of the lower sandwich (AFM)	–0.21
Mn in interstitial site	FM configuration	0.89
	AFM configuration	0.97

where the ejected Ga atom can come out and stay on the surface or in the interstitial between the sandwich. The difference between the total energy of the products and the reactants of the above equations (ΔE) give the formation energies that are reported in Table III. A negative value of the formation energy for a given configuration indicates that it is thermodynamically favorable. From our calculations, we find that Mn prefers to replace a surface Ga atom, with an energy gain of about -0.95 eV when the substituted Ga is pushed on the surface at a hollow site formed by the three surface Se atoms. We have also tried the configuration in which the substituted Ga is pushed on the surface on a Se-Se bridge site. However, after geometry optimization, the Ga atom moves to the above mentioned hollow site. The second most thermodynamically favorable position is when Mn substitutes a Ga atom in the second layer of the sandwichlike unit (energy gain -0.64 eV) and the substituted Ga atom is intercalated between two sandwiches. In both these configurations, the Mn-Mn interaction is ferromagnetic (FM) in nature. However, we note that ΔE for the antiferromagnetic (AFM) configurations are also similar in energy to that of the FM one. This suggests that the exchange coupling between the two Mn ions is negligible at such low concentrations (Mn-Mn distance being 11.24 Å). The other defect configurations, namely the Mn adsorbed on the surface, Mn in the interstitial site, and Mn intercalated between two GaSe sandwiches are less probable with respect to the substitutional cases. Except for the intercalated configuration, the FM is the more favorable magnetic configurations in these defects. For the intercalated one, we find that the AFM configuration is favored over the FM one.

B. Core level photoemission of the $Ga_{1-x}Mn_xSe$ alloy

After the preliminary work so far described, we have been able to identify the spectroscopic signatures of the conditions where the alloying process, yielding $Ga_{1-x}Mn_xSe$, was dominant over the Mn segregation on the surface. The Mn evaporation was repeated on freshly cleaved GaSe surfaces and, after Mn evaporation, annealing at 400 °C in ultrahigh vacuum was also carried out to further induce the alloying process through diffusion. The amount of evaporated Mn (4.6 ML) exceeds the overall amount of Mn of Sec. III A by a factor 1.2, and a larger contribution of metallic Mn is expected before annealing. However, the larger amount of Mn allowed us to collect data with a better statistics and obtain a good reference Mn $2p$ XPS spectrum of the Mn:GaSe alloy after the annealing treatment.

Figure 5 shows the Mn $2p$ core line of the Mn:GaSe interface prior and after annealing in vacuum. As observed, the four spectral features of the vacuum annealed interface present strong satellites (B and D) on the high BE side of the main lines (A and C) of the Mn $2p$ spin-orbit split components.

We can exclude the presence of relevant oxygen contaminations, as the measured Mn $2p$ XPS line shape is quite different from that of MnO [Fig. 5(d)]. Furthermore, we did not observe any signal from oxygen within the sensitivity of our probe. The spectrum of the as-deposited film [Fig. 5(b)] shows two broad spin-orbit split components, suggesting the presence of several contributions that could be ascribed to both metallic Mn and Mn diluted in the GaSe lattice. In fact, a comparison with the Mn $2p$ XPS core line from metallic Mn [Fig. 5(a)] indicates that the M1 and M2 features (marked by dashed vertical lines) can be ascribed to metallic Mn. These features are progressively quenched with annealing treatments

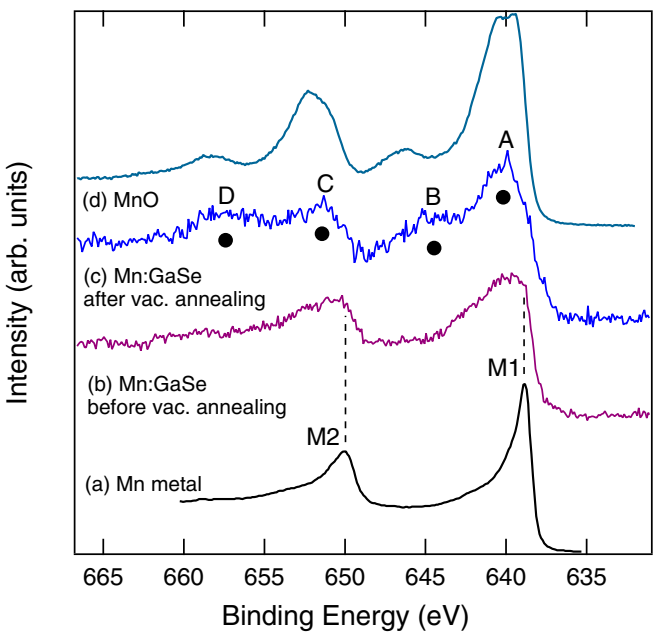

FIG. 5. XPS spectra of the Mn $2p$ core lines collected from (a) a thick Mn metallic film, (b) the Mn:GaSe interface before UHV annealing, (c) Mn:GaSe interface after UHV annealing, and (d) a MnO single crystal.

[Fig. 5(c)], indicating that the annealing is quite effective to prevalently induce a substitution of Ga by Mn atom, rather than a clustering of Mn on the GaSe(0001) surface.

The peaks A and C are separated by the spin-orbit interaction and the width of these two peaks can be ascribed to disorder effects, related to the replacement of Ga atom by Mn. On the high BE side of these peaks, the two (B and D) satellites are quite similar to those found in other Mn-based DMS, such as $Cd_{1-x}Mn_xTe$, $Zn_{1-x}Mn_xS$, and $Ga_{1-x}Mn_xAs$ [44,70,71]. They are ascribed to charge transfer effects from the ligand anions (Te, S, or As, respectively) to the $3d$ levels of Mn cations. These effects are usually accounted for in the frame of a configuration interaction (CI) model where the electronic states involved in the photoemission process are described by a linear combination of several configurations (see, e.g., Ref. [71] and references therein) such as $3d^n$, $3d^{n+1}\underline{L}$, and $3d^{n+2}\underline{L}^2$, where $\underline{L}$ represents a hole in the ligand created by the charge transfer process. The ligand-to-$3d$ charge-transfer energy is defined by $\Delta = E(3d^{n+1}\underline{L}) - E(3d^n)$. The intensity of B and D satellites varies depending on the charge transfer energy Δ, as well as on the hybridization strength (T) between the ligand orbitals and the Mn $3d$ orbitals involved in the charge transfer process. Therefore the line-shape analysis of the Mn $2p$ core levels shown in Fig. 5 provides an evidence of hybridization effects of Mn ions with atoms in the host lattice. In Sec. III D, a detailed calculation of the Mn spectral weight in photoemission through CI models will be carried out for the $3d$ levels in the valence-band region.

Finally, it is rather important to compare the present results with those obtained on the Fe-GaSe interface [49,50]. The analysis of Fe $2p$ XPS lineshape in the Fe-GaSe interface does not provide evidence of Fe-Se hybridization, being the Fe $2p$ XPS spectra quite similar to that of metallic Fe, while Fe clustering effects are found to be dominant. In turn, our measurements on the electronic properties of the Mn:GaSe interface have shown the capability of Mn to diffuse into the lattice, displaying remarkable hybridization effects with the atoms of the host lattice.

The results so far presented are consistent with the formation of a reacted $Mn_xGa_{1-x}Se$ interface at the early stages of growth. When further diffusion processes are hindered, a Mn overlayer is found to appear on the surface, consistently with the analysis displayed in Fig. 4.

C. X-ray absorption from the $Ga_{1-x}Mn_xSe$ alloy

The Mn L-edge XAS spectra are shown in Fig. 6. In particular, the data obtained after the Mn deposition (e) and after annealing at 400 °C and collected at RT (d) are presented. The as-deposited Mn-doped GaSe (e) shows the presence of both metallic and a reacted Mn-GaSe interface, as appearing from an overall smooth XAS lineshape, with minor modulations that will ultimately evolve into the post-annealing XAS lineshape (d). Indeed, after annealing at 400 °C, sharper features (labeled as A, B, C, D, and E) appear, and the comparison with multiplet calculations for a Mn^{2+} $2p^63d^5 \rightarrow 2p^53d^6$ electric-dipole allowed transition (c) unambiguously shows that the measured spectrum can be ascribed to a Mn^{2+} ion in the GaSe matrix.

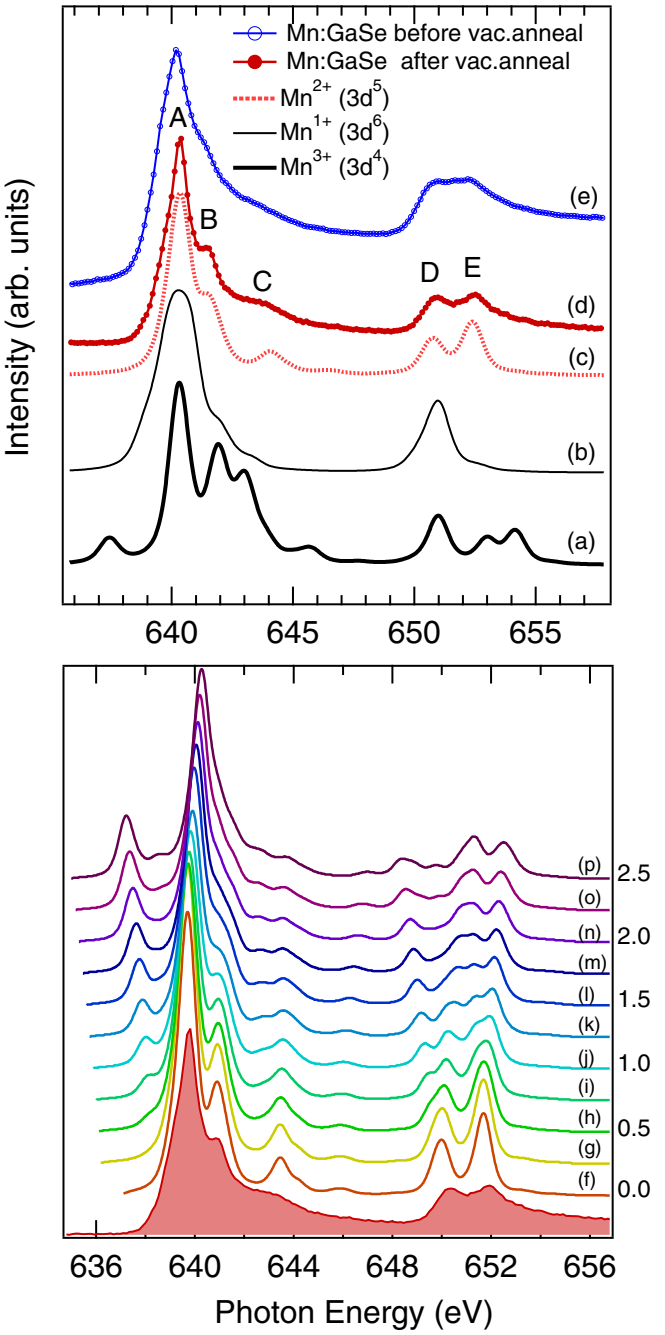

FIG. 6. (Top) Experimental Mn L-edge XAS spectra of Mn deposited on GaSe surface before annealing (e) and after annealing (d). Calculated atomic Mn L-edge XAS spectra (zero crystal field) for the +3 oxidation state of Mn ($3d^4$) (a), +1 oxidation state ($3d^6$) (b), and +2 oxidation state ($3d^5$) (c). (Bottom) Comparison between the experimental XAS spectrum of the annealed Mn:GaSe interface (shaded area) and the calculated XAS spectrum for the atomic Mn^{2+} $3d^5$ configuration with a tetrahedral crystal field 10Dq ranging from 0.0 to 2.5 eV.

Similar calculations for the Mn^{1+} (b) and Mn^{3+} (a) ions alone do not match the measured XAS spectrum, which is indeed already well reproduced by the calculations for atomic Mn^{2+}. However we cannot exclude that valence states different from 2+ can to a minor extent contribute to the XAS spectrum. This possibility was discussed in, e.g., Mn-doped GaAs

(Ref. [72] and references therein), where though Mn^{2+} was found to give the major contribution (60.8%) to the Mn L-edge XAS spectrum, also Mn^{3+} (10%) and Mn^{1+} (26.5%) were predicted to contribute to the spectral weight. According to Edmonds *et al.* [72], the contribution of multiple configurations (namely, $3d^4$, $3d^5$, $3d^6$) is allowed by the finite value of the hybridization energy (denoted as V in Ref. [72]) allowing the d occupation to fluctuate over the different d^n configurations. As compared to $Ga_{1-x}Mn_xAs$, in Mn-doped GaSe the Mn XAS profile is much closer to Mn^{2+}, with sharp features that, in turn, are much smeared out in GaAs due to configuration mixing. Furthermore, also the larger U and Δ energies with respect to the GaAs case make d^n fluctuations in Mn-doped GaSe less probable, consistently with the observed spectrum.

The remarkable similarity with the XAS spectrum predicted for the Mn^{2+} calculation is particularly helpful for the interpretation of the electron spectroscopy results. This will justify the assumption at the basis of CI calculations for the Mn $3d$ spectral weight in the valence band (see next section) where an Mn^{2+} ion will be assumed as the ionic configuration in the parameterized CI model.

In the bottom panel of Fig. 6, we have shown a set of calculated Mn XAS spectra in a tetrahedral T_d symmetry, starting from zero crystal field to 10Dq = 2.5 eV, where 10Dq is the crystal-field (CF) splitting of the $3d$ orbitals. It is important to note that crystal-field effects seem to be rather limited up to 10Dq = 0.75 eV. At this energy, two features appear on the low photon energy sides of the calculated Mn L_{III} and Mn L_{II} edges, that have no counterpart in the experimental data. Therefore we assume that crystal-field effects are negligible. This remark will also be at the basis of the CI model for the valence-band calculations, where crystal-field splitting will be set to 0.25 eV. The negligible tetrahedral crystal field suggests that also the effects of the trigonal distortions expected for the Mn ion substitutional in a Ga site could be negligible, and therefore will not be further considered in the present study.

D. Valence-band resonant photoemission at the Mn *L* edge

The valence-band spectra of the clean GaSe and of the Mn-doped, annealed, GaSe single crystals are shown in Fig. 7(a). The photoemission spectra have been collected with a photon energy of $h\nu = 797$ eV and have been normalized to the maximum of the valence-band emission (peak A). Both spectra show a main line with three features labeled A′, A, and B, and a peak C at higher binding energies. When Mn is evaporated on the GaSe cleaved surface, the main changes that can be observed are the appearance of a feature A″ at the Fermi edge, and an increase of the spectral weight in the regions between the peaks A and B and the peaks B and C.

Before we go into the interpretation of the experimental spectra based on our *ab initio* calculations, it would be important to understand the bulk band structure and the nature of the bonding in ϵ-GaSe and compare the later with that of the most widely studied zinc blende structure of GaAs. As shown in Fig. 1, in bulk GaSe, the Ga atoms are in a tetrahedra formed by three Se atoms in a plane and a Ga atom. The Ga-Se bond lengths are 2.47 Å and the Ga-Ga bond length is 2.43 Å. The computed bulk band structure

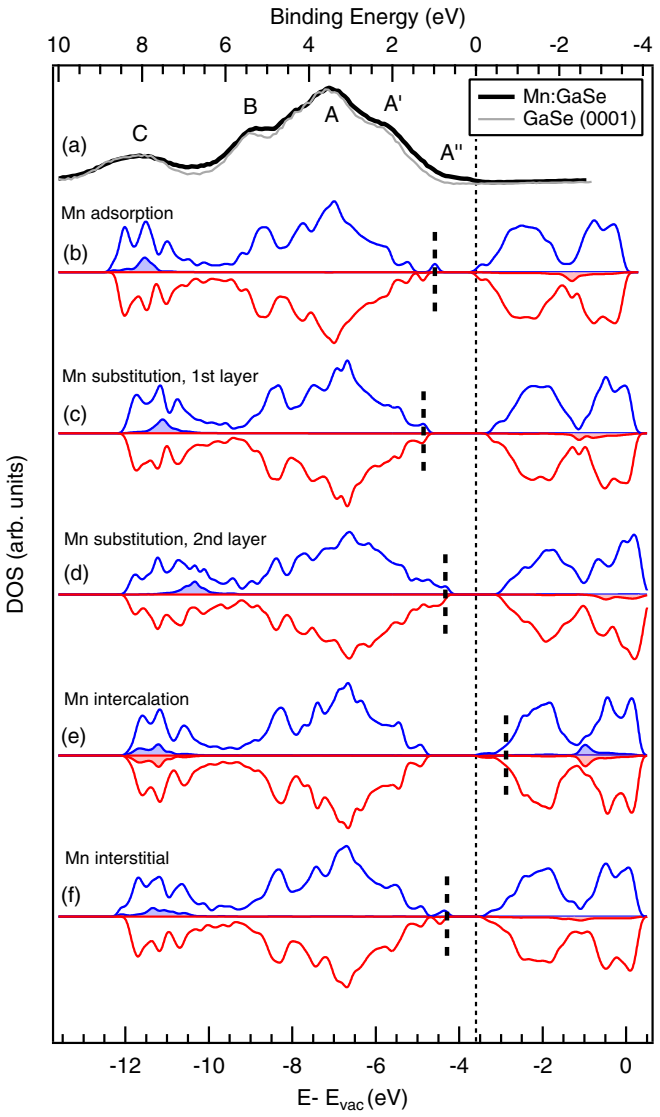

FIG. 7. Valence-band spectra of the clean GaSe (thin line) and the reacted Mn-GaSe surface (thick line) (a). Spin-projected DOS calculated for Mn adsorbed on the surface (b), Mn replacing Ga in the first Ga layer below the surface (c), Mn replacing Ga in the second Ga layer below the surface (d), Mn intercalated between the two Se layers (e), and Mn interstitial (f). Top-half: spin-up, bottom half: spin down; the Mn partial DOS is represented by shaded areas. The vertical dashed lines represent the calculated highest occupied states.

and density of states (DOS) are shown in Fig. 8(a). Both the band structure and the DOS are in reasonably good agreement with previous calculations [9,28]. We find a direct band gap of 0.98 eV at the Γ point of the Brillouin zone (BZ). We note that this is in agreement with that obtained by Ma *et al.* [9]. However, the corresponding experimental gap is 2.12 eV [10]. Underestimation of band gap is a common feature of DFT calculation. The valence band can be divided into three regions (I, II, and III) (Fig. 8). From the analysis of the projected DOS (PDOS), we find that the majority contributions to the DOS in region I and II come from the p states of Se and Ga (contributions from Se being higher than those of Ga). In region III, the dominant contributions come from the Ga s

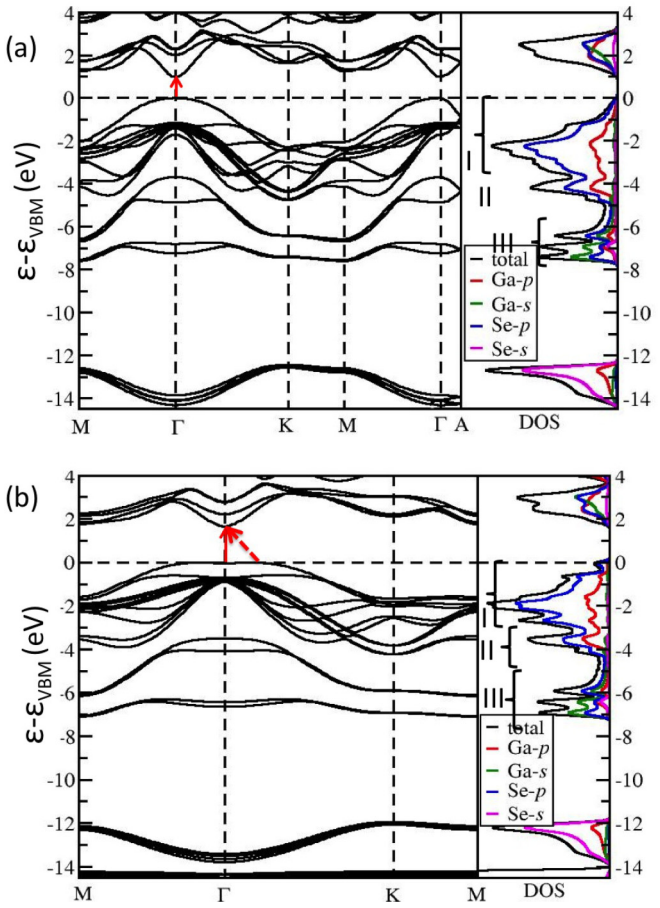

FIG. 8. Computed band structure (along $M \rightarrow \Gamma \rightarrow K \rightarrow M \rightarrow \Gamma \rightarrow A$ high-symmetry directions, please refer to Fig. 2 of Ref. [28] for the diagram of the Brillouin zone) and density of states (DOS, total of as well as projected on to the Ga and Se s and p states) of (a) bulk ϵ-GaSe and (b) the 0001 surface. The solid red arrows show the direct band gap at Γ while the dashed arrow shows the indirect band gap for the surface.

states that are hybridised with the Se p. Also there are some contributions from Se s. In order to understand the nature of bonding between Ga-Se and Ga-Ga, we have calculated the difference between the charge density for the interacting system and that obtained from superposition of atomic charge density for bulk ϵ-GaSe ($\Delta\rho$). The isosurfaces of $\Delta\rho$ are shown in Fig. 1(c). Yellow and green lobes indicate accumulation and depletion of electrons, respectively. In both sandwiches, we see that there is accumulation of charge between the atoms, while depletion from the atoms (for Se we see both accumulation and depletion), suggesting the covalent nature of the bonding between the atoms. On Se we see that there is a slight accumulation of charge (0.33 electrons). The Ga-Ga-Se bond angle and Ga-Se-surface normal bond angles are 118.8° suggesting that there is a mixture of sp^2 and sp^3 type of hybridization in this material. This is in contrast to GaAs where it is purely sp^3 hybridization.

The band structure and DOS of the (0001) surface in shown Fig. 8(b). The overall electronic structure is similar to that of the bulk except that the dispersion of the bands, particularly those in region I and II, are flatter than that of the bulk. The DOS has a new peak corresponding to the valence-band maxima (VBM). This peak arises from the flat surface states along the $M \rightarrow \Gamma \rightarrow K$ direction of the BZ. Further, on the surface, the band gap changes from a direct to an indirect one. The magnitude of the band gap increases to 1.66 eV compared to that of 0.98 eV in bulk. Our results are in good agreement with those reported in Ref. [9] where they have studied the variation of the band structure as a function of the number of sandwiches and have shown that for all the cases in which there is a surface, the band gap is an indirect one. Additionally, the width of the valence band comprising of regions I and II is reduced by about 0.68 eV.

The main features of the present experimental data can be interpreted on the basis of the calculated density of states (DOS) for the N-electron ground state of GaSe, which agree well with the results reported so far [28,73,74]. Indeed, the observed experimental peaks have a counterpart in the calculated DOS [Fig. 7(b)–7(f)]. Similar to the computed DOS, we identify three regions (I, II, and III) in the valence band. Region I corresponds to the observed peaks A and A′, region II to peak B and region III to peak C. On doping the sample with Mn followed by annealing, one would expect a decrease in the spectral weight in region III if Mn is substituting Ga. Indeed, we observe such a reduction in our valence-band spectra corresponding to peak C (Fig. 7) suggesting that Mn is substituting Ga atoms. Finally, the states appearing at the Fermi edge (A″) could be ascribed to the hybridization of the Mn s and p states with the Se p states as explained below.

A careful analysis of the occupation of the Mn d orbitals show that they are half-filled. Our calculations suggest that Mn is in the +2 oxidation state which is in agreement with that obtained from the XAS spectra reported in Fig. 6. The magnetic moment on the Mn ions varies between 4.73–4.83 μ_B depending on the local environment they are in. When Mn is replacing a Ga atom on the surface layer (this is thermodynamically the most favourable one) the magnetic moment of the Mn atom is 4.77 μ_B. We note that these values are slightly different from 5.0 μ_B, had Mn been in its +2 oxidation state; this departure being due to the hybridization with the neighboring Se and Ga atoms.

The structure and the DOS projected on the Mn d, s and p, Se p, and Ga s and p orbitals for the substitutional configurations, namely, the cases where the Mn atom is replacing the Ga atom, either in the first or in the second layer, are shown in Figs. 9 and 10, respectively. In both the cases, the Mn atom is in a tetrahedron whose base is formed by three Se atoms and the vertex is a Ga atom (Fig. 9). The Se atoms form a triangle that is slightly distorted from an equilateral one. For Mn substituting the Ga atom in the first layer (second layer), the two Se-Se distances are 4.00 and 3.96 Å (4.07 and 3.98 Å). There are two types of Mn-Se bond, two shorter bonds of length 2.58 Å (2.62 Å) and one longer one of 2.63 Å (2.58 Å) for Mn substituting the Ga atom in the first layer (second layer). The departure from the expected C_{3v} symmetry is due to the presence of the popped out Ga atom that has been replaced by Mn. The Ga-Mn bond lengths for the two cases are 2.58 and 2.56 Å, respectively. Both the Mn-Se and Mn-Ga bond lengths are longer compared to that of Ga-Se and Ga-Ga, suggesting weaker bonding of the Mn ions in the GaSe lattice.

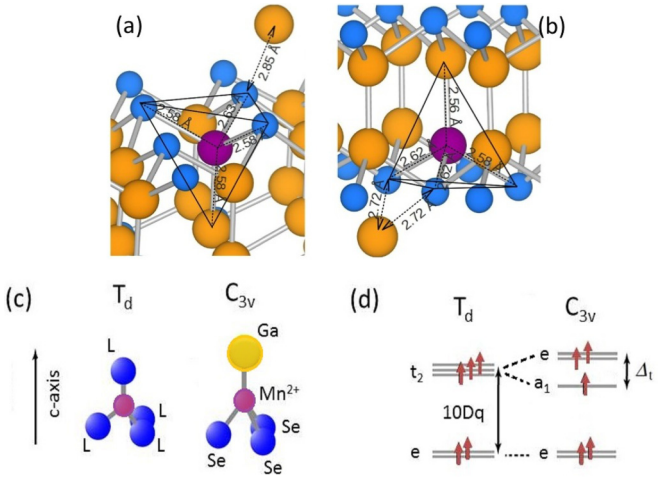

FIG. 9. Local structure of Mn replacing Ga atom in the first layer (a) and the second layer (b). The blue, magenta and yellow spheres represent Se, Mn and Ga atoms, respectively. Schematic energy level diagram (not to scale) of the effects of cluster distortions from T_d to C_{3v} (c) on the Mn 3*d* levels energies (d). 10Dq is the tetrahedral crystal-field splitting, while Δ_t is the splitting due to the trigonal distortion.

The DOS of the occupied region (Fig. 10) can be split into two regions: (i) between −13 and −10 eV and (ii) between −10 eV to the highest occupied state. The occupied Mn-d states are primarily localized in region (i). The Mn atom is in a C_s symmetry resulting in all the five *d* orbitals being nondegenerate. However, compared to conventional DMS (for example, Mn doped GaAs) the effect of crystal-field splitting is negligible here. This is because in typical cases, the Mn atom is surrounded by the ligand atoms, while here we have a Ga atom and the electronegativity difference between the Mn and Ga is much less compared to that of Mn and the ligands resulting in less ionicity of the bonds. Moreover, in typical DMS where the host material has diamondlike or zinc-blende structures, the dopant *d* orbitals hybridize primarily with the anion (ligand) *s* and *p* orbitals. However, in the case of Mn-doped GaSe, we find that the hybridization of Mn *d* with the Se *s* and *p* orbitals is weak. Instead, there is hybridization (still weak but stronger than that with Se states) of Mn *d* with Ga *s* at the bottom of the valence band. In particular from the projected DOS in Fig. 10 we see that in the region (i), the peaks of the DOS projected on Ga *s* states follow those projected on the Mn d_{z^2} (denoted by red arrows in the Fig. 10). In region (ii), the contributions to the states in both the spin up and down channel are primarily from the Se and Ga *p* states hybridized with the Mn *p* and *s* states. We note that for the doped system, the valence band edge states result from the mixing of the Mn *p* and *s* with *p* states of Se and *s* and *p* states of Ga. This results in an increase in states appearing at the Fermi edge (A″) in the experimental valence-band spectra (Fig. 7). This is in contrast with that of Mn doped GaAs where it is still not clear whether the Mn impurity band is merged with the valence band [75] or detached from it [76]. From the DOS, it is also evident that unlike in Mn-doped GaAs, there is no hole doping in our system. As Mn is the open-shell magnetic ion in the Mn:GaSe system, which is expected to carry a magnetic moment through

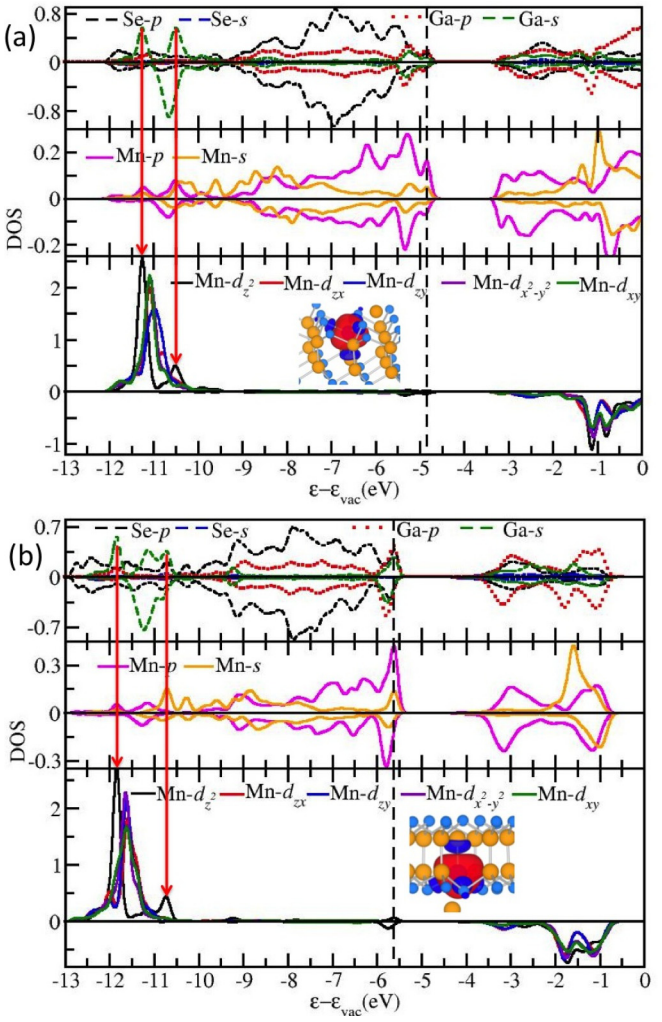

FIG. 10. Density of states projected on the Mn-*d*, and on Se *p* and Ga *s* and *p* orbitals for (a) Mn replacing the surface Ga atom and (b) Mn replacing a Ga atom in the second layer of the sandwich, both in their FM configuration. The positive and negative values of the DOS indicates spin up and spin down channels. The inset shows the isosurfaces of magnetization densities. The blue and yellow spheres denote Se and Ga atoms respectively. Red and deep blue isosurfaces represent spin up and spin down, respectively. The black, vertical dashed lines denote highest occupied states. All the energy eigenvalues are aligned with respect to the energy at vacuum, which has been set to zero. The red arrow indicates the overlap of the Mn-d_{z^2} peak with the Ga-*s*.

the Mn 3*d* electrons, a ResPES study across the Mn 2*p*-3*d* absorption edge has been carried out in order to enhance the Mn contribution to electronic states in the valence-band region.

The results are shown in Fig. 11. On the XAS spectrum (top panel) the photon energies (a to j) selected to collect ResPES data are indicated. The whole set of ResPES data is shown in the bottom panel. The data span a photon range across the Mn L_{III} threshold. The VB spectra show a clear enhancement of the spectral weight at a photon energy of about 640 eV. At this energy a peak around BE = 4.5 eV in the valence band shows a remarkable intensity enhancement. The difference between the resonant (e) and off-resonance (a) spectra (hereafter denoted as resonating spectral weight, RSW) is also shown in the bottom

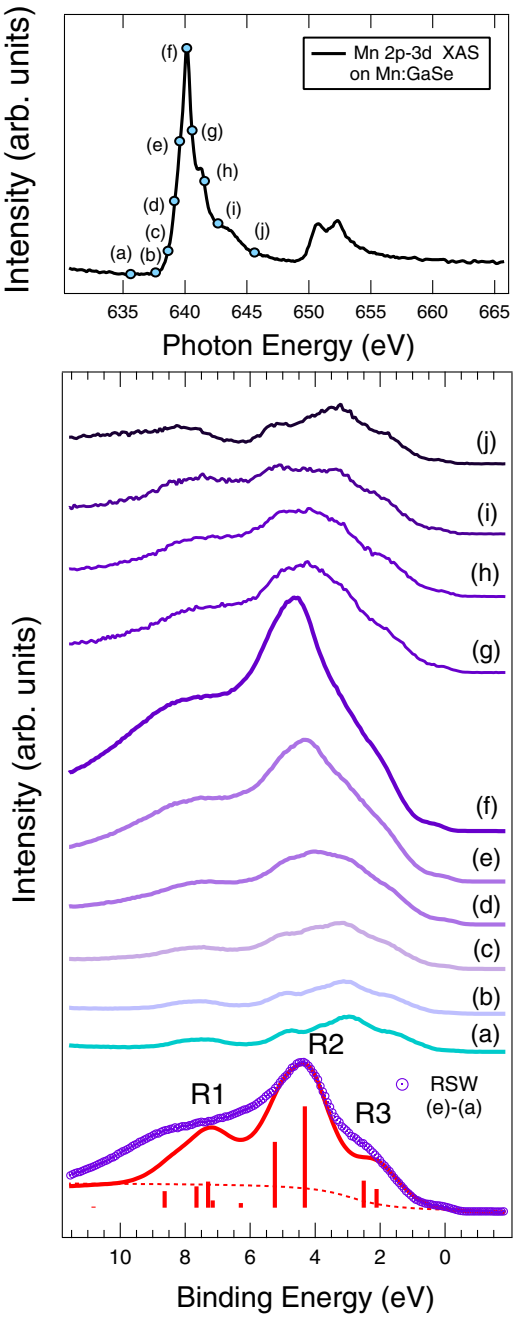

FIG. 11. (Top) XAS spectrum of the Mn-GaSe interface collected at the Mn $2p$-$3d$ edge. The dots indicate the photon energies chosen to collect the, resonant, valence-band photoemission spectra. (Bottom) Set of valence-band spectra collected at different photon energies across the Mn $2p$-$3d$ edge. Resonant spectral weight (RSW, x 1.30) obtained from the difference between the resonant VB spectrum (e) and the off-resonance spectrum (a) collected at 639.5 and 635.5 eV, respectively. Dashed line: simulated integral background. Thick line: calculated Mn $3d$ spectral weight. Vertical bars: calculated intensities corresponding to the eigenenergies of the final state.

panel. Here it is clearly seen that the RSW is determined by a peak at 4.5 eV (R2) and by two broad features at about BE = 6–8 eV (R1) and BE = 1–3 eV (R3).

We have used spectrum (e) rather than (f), as it is known [77] that for spectra collected with photon energies at the maximum of the absorption threshold [spectrum (f) in the present case] the weight of the Auger emission channel is not negligible and the maximum of the valence-band emission is already shifted to higher BE with respect to spectrum (e), where the resonant Raman Auger channel (RRAS) is still dominant.

Further insight into the origin of the three spectral features (R1, R2, and R3) in the RSW can be obtained at the light of parameterized CI calculations for the valence-band photoemission. The Mn RSW cannot be directly compared to the calculated DOS, as the latter are carried out for the N-electron ground state, while the RSW refers to the $N-1$ electron spectral weight of the photoemission process final state. For open shell systems, a remarkable difference is expected between DFT+U ground-state calculations and photoemission, due to relevant multiplet splitting and charge transfer process occurring upon photoemission from the open shell transition metal cation. However, the CI analysis will help us to retrieve the Hubbard d-d correlation energy and the charge transfer energy parameters to be compared with *ab initio* predictions of the electronic properties.

For the CI cluster calculations, we considered the most energetically favorable configurations resulting from the theoretical calculations, i.e., Mn substitutional in the first and second Ga layers. Actually, for Mn substitution of Ga in the second layer, we assume that Mn $3d$ states hybridize with Se cations at the bottom and with a Ga atom on top. When Mn replaces Ga in the topmost layer, three Se atoms are found above Mn and one Ga atom below it. These geometries are described in Fig. 9. The symmetry of the ($GaSe_3$)Mn cluster is C_{3v}, which can be assumed as a distortion of the T_d symmetry, mainly due to the presence of Ga at one of the tetrahedron vertex. Strictly speaking, the slightly different bond lengths should further lower the cluster symmetry from C_{3v} to C_s, as shown in Fig. 9, based on the results of the theoretical calculations. If a crystal-field approach is considered, the lowering of the cluster symmetry from T_d to C_{3v} partially removes the threefold degeneracy of the T_2 energy level which split in a twofold degenerate E level and in a nondegenerate A level [see Figs. 9(c) and 9(d)]. On the basis of the XAS data, we concluded that the distortion leading to the T_d and ultimately to the C_{3v} symmetry have negligible effects on the electron spectroscopy spectra, as the XAS spectrum was very similar to the atomic case. In addition, we wish to recall that crystal-field effects are known to be smaller in T_d than in O_h symmetry [79]. For this reason, we adopted a low tetrahedral CF in the CI calculations (10Dq = 0.25 eV, see comment below). A low crystal field is also expected to yield high-spin configurations [79]. This assumption is consistent with our computational results, which show that the magnetic moment for Mn ions is quite close to 5. In any case, the splitting of T_2 and E orbital energy in the calculations is also determined by the different hybridization with the ligand orbitals, which is accounted for by the v_σ and v_π transfer integrals (which ultimately account for the ligand field effects, as they appear in the off-diagonal terms of the model Hamiltonian to parametrize the hybridization between ionic and charge-transfer derived configurations), usually defined through the $(pd)_\sigma$ and $(pd)_\pi$ Slater-Koster integrals [80], as properly described in Ref. [81]. Following this reference, we set $v_\sigma = -\sqrt{3}(pd)_\sigma$ and $v_\pi = -2(pd)_\pi$. In this frame, the undistorted T_d geometry with

small or negligible crystal field on the Mn^{2+} ion, but with the proper symmetry-adapted transfer integrals, was assumed as an effective approximation for the local environment of Mn. Our assumption is corroborated by the results obtained from other cubic Mn-doped DMF [78,82–84], where the Mn 3*d* spectral weight in the valence band look very similar, and differences are mostly determined by the extent of the ligand-to-Mn charge transfer energy parameter.

In the CI calculations, we assume that Ga behaves as a ligand in the $(GaSe_3)Mn$ cluster. This assumption is justified by the hybridization between the Ga *s* state and the Mn d_{z^2} states disclosed by our *ab initio* calculations. Here, the CI model is meant to be an effective model that provides a guideline to interpret the main features of the resonant Mn 3*d* spectral weight. At this stage, the model does not include lattice distortion leading to lower symmetries (C_{3v} or C_s) as these distortions are relatively small, and does not include different hybridization of Mn with Ga or Se.

Impurity-cluster CI calculations of the Mn 3*d* spectral weight are shown in the bottom of Fig. 11. On the basis of the $3d^{n+m}\underline{L}^m$ configurations ($\underline{L}$ denotes a ligand hole) used to describe the open shell of the 3*d* transition metal ion during the photoemission process, the spectral weight in a photoemission experiment was calculated, in the sudden approximation, by projecting the final state configurations ($|\Psi_{i,fs}\rangle$) on the ground state, i.e.. $I_{\mathrm{XPS}}(\mathrm{BE}) \propto \sum_i |\langle\Psi_{\mathrm{GS}}|\Psi_{i,fs}\rangle|^2\delta(BE-\varepsilon_i)$. Here, $|\Psi_{\mathrm{GS}}\rangle$ represents the ground state (GS) wave function, and the sum is run over all final state configurations $|\Psi_{i,fs}\rangle$ with energy ε_i. Where required, proper fractional parentage coefficients can be used, as was done in the present case.

The calculations (shown in the bottom panel of Fig. 11) have been carried out following the scheme presented by Fujimori *et al.* [78] for several Mn doped semiconductors, based on a $3d^5$ initial state of the transition metal atom [81]. The parameter set used in the calculation is $10\mathrm{Dq} = 0.25$ eV for the CF splitting, $\Delta = 2.95$ eV for the charge transfer energy, $U = 6.4$ eV for the *d*-*d* correlation energy (which well compares with the *ab initio* calculated $U_{\mathrm{eff}} = 5.84$ eV value), and $pd\sigma = -1.25$ eV for the hybridization integral. The free ion Racah parameters for Mn^{2+}, $B = 0.126$, $C = 0.421$, were also considered.

As mentioned above, the sequence of the three broad R1, R2, and R3 RSW peaks observed for the nearly-2D Mn-GaSe system is a common feature shared by many Mn-based DMS [78,82–84] with a 3D zincblende crystal structure. It is known that the relative intensity of R1 and R3 depends on the bond ionicity of the host lattice, and the intensity of R1 is found to increase with respect to R3 as the anion-cation bonding in the host lattice becomes less ionic (e.g. going from $Zn_{1-x}Mn_xS$ to $Zn_{1-x}Mn_xSe$ and finally to $Zn_{1-x}Mn_xTe$ [85], or from $Cd_{1-x}Mn_xS$ to $Cd_{1-x}Mn_xSe$ and finally to $Cd_{1-x}Mn_xTe$ [78]). Among the three features observed in the RSW, R1 receives a larger contribution from $3d^4$ configuration in the final state, while the $3d^5\mathrm{L}$ configurations are the one mostly contributing to R2 and R3 spectral features. The strong similarities between GaSe and the 3*d* zinc-blende DMS seem to indicate that the Mn-related states contributing to the valence band are weakly affected by the long-range crystal order, as they are mainly determined by the local Mn coordination. Finally, we observe that calculations of the Mn 3*d* VB spectral weight where CF increases from 0.0 eV up to 1.25 eV (see Ref. [86], part 2.) show that low CF values are required to catch the main experimental features. CFs above about 0.25 eV yield a redistribution of spectral weight and relative energies between peaks far from the experimental data. Namely, a decrease of peak R3 intensity and an increase of peak R2 intensity are predicted, which bring the calculations far from the experimental data.

IV. CONCLUSIONS

We have been able to prepare well characterized Mn:GaSe interfaces, providing an evidence of the formation of a $Ga_{1-x}Mn_xSe$ reacted top layer at the early stages of growth, where Mn ions preferentially go into substitutional sites replacing Ga ions. Alloying is obtained already during evaporation at room temperature, without postgrowth annealing. Unlike Fe-GaSe interfaces, where iron clustering effects are dominant and no trace of Fe-Se hybridization is found upon the analysis of Fe $2p$ XPS line shape [49,50], our measurements on the electronic properties of the Mn:GaSe interface have shown the capability of Mn to diffuse into the lattice with detectable hybridization with the host lattice atoms. The Mn cation valence state is probed by XAS measurements at the Mn *L* edge, which show that Mn diffuses into the lattice as a Mn^{2+} cation with negligible crystal-field effects. This is supported by the DFT+U calculations that also predict a calculated magnetic moment close to 5 μ_B, expected for a Mn^{2+} ion in a low crystal filed with relatively low hybridization effects for the Mn 3*d* states. Finally, unlike other Mn-doped semiconductors, the calculations of the electronic structure indicate that (a) there is an interaction between the Ga-*s* and Mn d_{z^2} states and (b) the empty Mn *s* and *p* states hybridize with the ligand *p* and *s* states, while lower hybridization effects are found the Mn 3*d* orbitals, though characteristic satellites in photoemission spectra are detectable in both XPS and RESPES spectra.

ACKNOWLEDGMENTS

P.G. acknowledges CDAC Pune and Garuda India, and Center for Computational Materials Science, Institute for Materials Research, Tohoku University for computing facility and DST-Nanomission Project No. SR/NM/NS-15/2011 for funding.

[1] K. Kato and N. Umemura, Opt. Lett. **36**, 746 (2011).

[2] A. Segura, J. Bouvier, M. V. Andrés, F. J. Manjón, and V. Muñoz, Phys. Rev. B **56**, 4075 (1997).

[3] S. Nüsse, P. Haring Bolivar, H. Kurz, V. Klimov, and F. Levy, Phys. Rev. B **56**, 4578 (1997).

[4] H. Ertap, G. M. Mamedov, M. Karabulut, and A. Bacioglu, J. Lumin. **131**, 1376 (2011).

[5] P. A. Hu, Z. Z. Wen, L. F. Wang, P. H. Tan, and K. Xiao, ACS Nano **6**, 5988 (2012).

[6] H. Peng, S. Meister, C. K. Chan, X. F. Zhang, and Y. Cui, Nano Lett. **7**, 199 (2007).

[7] X. Song, J. Hu, and H. Zeng, J. Mater. Chem. C **1**, 2952 (2013).

[8] H. S. S. Ramakrishna Matte, B. Plowman, R. Datta, and C. N. R. Rao, Dalton Trans. **40**, 10322 (2011).

[9] V. Zólyomi, N. D. Drummond, and V. I. Fal'ko, Phys. Rev. B **87**, 195403 (2013).

[10] E. Aulich, J. L. Brebner, and E. Mooser, Phys. Solid State **31**, 129 (1969).

[11] Y. Peng, C. Xia, H. Zhang, T. Wang, S. Wei, and Y. Jia, Phys. Chem. Chem. Phys. **16**, 18799 (2014).

[12] L. Huang, Z. Chen, and J. Li, RSC Adv. **5**, 5788 (2015).

[13] Z. Chen, K. Gacem, and M. Boukhicha, J. Biscaras, and A. Shukla, Nanotechnol. **24**, 415708 (2013).

[14] L. Ao, H. Y. Xiao, X. Xiang, S. Li, K. Z. Liuc H. Huang, and X. T. Zu, Phys. Chem. Chem. Phys. **17**, 10737 (2015).

[15] T. Cao, Z. Li, and S. G. Louie, Phys. Rev. Lett. **114**, 236602 (2015).

[16] D. J. Late, B. Liu, J. J. Luo, A. M. Yan, H. S. S. R. Matte, M. Grayson, C. N. R. Rao, and V. P. Dravid, Adv. Mater. **24**, 3549 (2012).

[17] Michel Cote, Marvin L. Cohen, and D. J. Chadi, Phys. Rev. B **58**, R4277(R) (1998).

[18] Wei An, Feng Wu, Hong Jiang, Guang-Shan Tian, and Xin-Zheng, J. Chem. Phys. **141**, 084701 (2014).

[19] E. Scalise, M. Houssa, E. Cinquanta, C. Grazianetti, B. van den Broek, G. Pourtois, A. Stesmans, M. Fanciulli, and A. Molle, 2D Mater. **1**, 011010 (2014).

[20] T. M. Pekarek, B. C. Crooker, I. Miotkowski, and A. K. Ramdas, J. Appl. Phys. **83**, 6557 (1998).

[21] T. M. Pekarek, C. L. Fuller, J. Garner, B. C. Crooker, I. Miotkowski, and A. K. Ramdas, J. Appl. Phys. **89**, 7030 (2001).

[22] A. G. Petukhov, I. I. Mazin, L. Chioncel, and A. I. Lichtenstein, Phys. Rev. B **67**, 153106 (2003).

[23] T. C. Lovejoy, E. N. Yitamben, S. M. Heald, F. S. Ohuchi, and M. A. Olmstead, Appl. Phys. Lett. **95**, 241907 (2009).

[24] T. C. Lovejoy, E. N. Yitamben, S. M. Heald, F. S. Ohuchi, and M. A. Olmstead, Phys. Rev. B **83**, 155312 (2011).

[25] S. F. Dubinin, V. I. Maksimov, and V. D. Parkhomenko, Crystallogr. Rep. **56**, 1165 (2011).

[26] R. H. Tredgold, R. H. Williams, and A. Clark, Phys. Stat. Sol. (a) **3**, 407 (1970).

[27] M. Schlüter, Il Nuovo Cimento B **13**, 313 (1973).

[28] L. Plucinski, R. L. Johnson, B. J. Kowalski, K. Kopalko, B. A. Orlowski, Z. D. Kovalyuk, and G. V. Lashkarev, Phys. Rev. B **68**, 125304 (2003).

[29] D. V. Rybkovskiy, A. V. Osadchy, and E. D. Obraztsova, Phys. Rev. B **90**, 235302 (2014).

[30] D. V. Rybkovskiy, N. R. Arutyunyan, A. S. Orekhov, I. A. Gromchenko, I. V. Vorobiev, A. V. Osadchy, E. Y. Salaev, T. K. Baykara, K. R. Allakhverdiev, and E. D. Obraztsova, Phys. Rev. B **84**, 085314 (2011).

[31] S. Wu, X. Dai, H. Yu, H. Fan, J. Hu, and W. Yao, arXiv:1409.4733v2.

[32] A. V. Kosobutskya, S. Yu. Sarkisovc, and V. N. Brudnyib, J. Phys. Chem. Solids **74**, 1240 (2013).

[33] Y. Ma, Y. Dai, M. Guo, L. Yua, and B. Huang, Phys. Chem. Chem. Phys. **15**, 7098 (2013).

[34] S. Azatyana, M. Hiraib, M. Kusakab, and M. Iwamib, Appl. Surf. Sci. **237**, 105 (2004).

[35] J. Hirvonen Grytzelius, H. M. Zhang, and L. S. O. Johansson, Phys. Rev. B **78**, 155406 (2008).

[36] E. Magnano, F. Bondino, M. C. Mozzati, C. Cepek, and F. Parmigiani, Appl. Phys. Lett. **96**, 152503 (2010).

[37] C. Zeng, W. Zhu, S. C. Erwin, Z. Zhang, and H. H. Weitering, Phys. Rev. B **70**, 205340 (2004).

[38] W. Zhu, H. H. Weitering, E. G. Wang, E. Kaxiras, and Z. Zhang, Phys. Rev. Lett. **93**, 126102 (2004).

[39] P. De Padova, J.-P. Ayoub, I. Berbezier, P. Perfetti, C. Quaresima, A. M. Testa, D. Fiorani, B. Olivieri, J.-M. Mariot, A. Taleb-Ibrahimi, M. C. Richter, and O. Heckmann, and K. Hricovini, Phys. Rev. B **77**, 045203 (2008).

[40] H. M. Zhang, J. Hirvonen Grytzelius, and L. S. O. Johansson, Phys. Rev. B **88**, 045311 (2013).

[41] L. Sangaletti, D. Ghidoni, S. Pagliara, A. Goldoni, A. Morgante, L. Floreano, A. Cossaro, M. C. Mozzati, and C. B. Azzoni, Phys. Rev. B **72**, 035434 (2005).

[42] L. Sangaletti, E. Magnano, F. Bondino, C. Cepek, A. Sepe, and A. Goldoni, Phys. Rev. B **75**, 153311 (2007).

[43] A. Wall, A. Raisanen, G. Haugstad, and L. Vanzetti, and A. Franciosi, Phys. Rev. B **44**, 8185 (1991).

[44] L. Sangaletti, A. Verdini, S. Pagliara, G. Drera, L. Floreano, A. Goldoni, and A. Morgante, Phys. Rev. B **81**, 245320 (2010).

[45] E. Magnano, F. Bondino, C. Cepek, L. Sangaletti, M. C. Mozzati, and F. Parmigiani, J. Appl. Phys. **111**, 013917 (2012).

[46] J. L. Hilton, B. D. Schultz, and C. J. PAlmstrøm, J. Appl. Phys. **102**, 063513 (2007).

[47] Y. Ishida, D. D. Sarma, K. Okazaki, J. Okabayashi, J. I. Hwang, H. Ott, A. Fujimori, G. A. Medvedkin, T. Ishibashi, and K. Sato, Phys. Rev. Lett. **91**, 107202 (2003)

[48] J. I. Hwang, Y. Osafune, M. Kobayashi, K. Ebata, Y. Ooki, Y. Ishida1, A. Fujimori, Y. Takeda, T. Okane, Y. Saitoh, K. Kobayashi, and A. Tanaka, J. Appl. Phys. **101**, 103709 (2007).

[49] A. R. de Moraes, D. H. Mosca, W. H. Schreiner, J. L. Guimaraes, A. J. A. de Oliveira, P. E. N. de Souza, V. H. Etgens, and M. Eddrief, J. Magn. Magn. Mater. **272-276**, 1551 (2004).

[50] A. R. de Moraes, D. H. Mosca, N. Mattoso, J. L. Guimaraes, J. J. Klein, W. H. Schreiner, P. E. N. de Souza, A. J. A. de Oliveira, M. A. Z. de Vasconcellos, D. Demaille, M. Eddrief, and V. H. Etgens, J. Phys. Condens. Matter **18**, 1165 (2006).

[51] M. Yamamoto, H. Mino, I. Akai, T. Karasawa, and V. F. Aguekian, J. Lumin. **87-89**, 275 (2000).

[52] W. S. M. Werner, Surf. Int. Anal. **31**, 141 (2001).

[53] A. Jablonski, Phys. Rev. B **58**, 16470 (1998).

[54] G. Drera, G. Salvinelli, J. Åhlund, P. G. Karlsson, B. Wannberg, E. Magnano, S. Nappini, and L. Sangaletti, J. Electron Spectrosc. Relat. Phenom. **195**, 109 (2014).

[55] M. Zerrouki, J.-P. Lacharme, M. Ghamnia, C. A. Sébenne, and M. Eddrief, and B. Abidri, Appl. Surf. Sci. **166**, 143 (2000).

[56] S. A. Chambers, M. H. Engelhard, V. Shutthanandan, Z. Zhu, T. C. Droubay, L. Qiao, P. V. Sushko, T. Feng, H. D. Lee, T. Gustafsson, E. Garfunkel, A. B. Shah, J. M. Zuo, and Q. M. Ramasse, Surf. Sci. Rep. **65**, 317 (2010).

[57] G. Salvinelli, G. Drera, A. Giampietri, and L. Sangaletti, ACS Appl. Mater. Interfaces **7**, 25648 (2015).

[58] P. Giannozi *et al.*, J. Phys. Condens. Matter **21**, 395502 (2009).

[59] D. Vanderbilt, Phys. Rev. B **41**, 7892 (1990).

[60] J. P. Perdew, K. Burke, and M. Ernzerhof, Phys. Rev. Lett. **77**, 3865 (1996).
[61] N. Marzari, D. Vanderbilt, A. De Vita, and M. C. Payne, Phys. Rev. Lett. **82**, 3296 (1999).
[62] S. Grimme, J. Comp. Chem. **27**, 1787 (2006).
[63] V. Barone *et al.*, J. Comp. Chem. **30**, 934 (2009).
[64] H. Monkhorst and J. Pack, Phys. Rev. B **13**, 5188 (1976).
[65] S. Nagel, A Baldereschi, and K Maschke, J. Phys. C **12**, 1625 (1979).
[66] M. Cococcioni and S. de Gironcoli, Phys. Rev. B **71**, 035105 (2005).
[67] V. I. Anisimov, J. Zaanen, and O. K. Andersen, Phys. Rev. B **44**, 943 (1991).
[68] V. I. Anisimov, I. V. Solovyev, M. A. Korotin, M. T. Czyzyk, and G. A. Sawatzky, Phys. Rev. B **48**, 16929 (1993).
[69] I. V. Solovyev, P. H. Dederichs, and V. I. Anisimov, Phys. Rev. B **50**, 16861 (1994).
[70] L. Sangaletti, M. C. Mozzati, G. Drera, V. Aguekian, L. Floreano, A. Morgante, and A. Goldoni, and G. Karczewski, Appl. Phys. Lett. **96**, 142105 (2010).
[71] J. Okabayashi, A. Kimura, O. Rader, T. Mizokawa, A. Fujimori, T. Hayashi, and M. Tanaka, Phys. Rev. B **58**, R4211 (1998).
[72] K. Edmonds G. van der Laan, and G. Panaccione, Semicond. Sci. Technol. **30**, 043001 (2015).
[73] Zs. Rak, S. D. Mahanti, Krishna C. Mandal, and N. C. Fernelius, J. Phys. Chem. Solids **70**, 344 (2009).
[74] M. O. D. Camara, A. Mauger, and I. Devos, Phys. Rev. B **65**, 125206 (2002).
[75] I. Di. Marco, P. Thunstrom, M. I. Katsnelson, J. Sadowski, K. Karlsson, S. Lebegue, J. Kanski, and O. Eriksson, Nat. Commun. **4**, 2645 (2013).
[76] M. Dobrowolska, K. Tivakornsasithorn, X. Liu, J. K. Furdyna, M. Berciu, K. M. Yu, and W. Walukiewicz, Nat. Mat. **11**, 444 (2012).
[77] See, e.g., L. Sangaletti, S. Dash, A. Verdini, L. Floreano, A. Goldoni, G. Drera, S. Pagliara, and A. Morgante, J. Phys. Condens. Matter **24**, 235502 (2012), and Refs. therein.
[78] T. Mizokawa and A. Fujimori, Phys. Rev. B **48**, 14150 (1993).
[79] See, e.g., R. G. Burns, *Mineralogical Applications of Crystal Field Theory*, 2nd ed. (Cambridge University Press, Cambridge, 1993).
[80] J. C. Slater and G. F. Koster, Phys. Rev. **94**, 1498 (1954).
[81] A. Fujimori, M. Saeki, N. Kimizuka, M. Taniguchi, and S. Suga, Phys. Rev. B **34**, 7318 (1986).
[82] J. I. Hwang, Y. Ishida, M. Kobayashi, H. Hirata, K. Takubo, T. Mizokawa, A. Fujimori, J. Okamoto, K. Mamiya, Y. Saito, Y. Muramatsu, H. Ott, A. Tanaka, T. Kondo, and H. Munekata, Phys. Rev. B **72**, 085216 (2005).
[83] J. Okabayashi, T. Mizokawa, D. D. Sarma, A. Fujimori, T. Slupinski, and A. Oiwa, and H. Munekata, Phys. Rev. B **65**, 161203(R) (2002).
[84] J. Okabayashi, A. Kimura, T. Mizokawa, A. Fujimori, and T. Hayashi, and M. Tanaka, Phys. Rev. B **59**, R2486(R) (1999).
[85] T. Mizokawa, T. Nambu, A. Fujimori, T. Fukumura, and M. Kawasaki, Phys. Rev. B **65**, 085209 (2002).
[86] See Supplemental Material at http://link.aps.org/supplemental/10.1103/PhysRevB.93.115304 for the details of the dipole corrections introduced in the calculations of the Mn-doped GaSe slab and for crystal-field dependent impurity cluster calculations of the Mn 3*d* spectral weight in the valence band.